Fused Filament Fabrication of Void-Free Parts using Low Viscosity Hot Melt Adhesives

Masoumeh Pourali and Amy M. Peterson*
University of Massachusetts Lowell, Department of Plastics Engineering, Lowell, MA, United States
*Corresponding Author
Email Address: Amy_Peterson@uml.edu

Abstract

In this work, a polyamide hot melt adhesive was evaluated as a feedstock for material extrusion additive manufacturing (AM). This adhesive, Technomelt PA 6910, is a semicrystalline polymer with a sub-ambient glass transition temperature, intermediate melting temperatures, and low recrystallization temperature. Due to this combination of properties, Technomelt PA 6910 is a room temperature flexible material that exhibits high toughness and strength, and good adhesion. Technomelt PA 6910 was extruded into filament form and printed using fused filament fabrication (FFF), a desktop form of material extrusion AM. The effect of extruder temperature on print quality and mechanical properties and the effect of raster angle and layer height on mechanical properties of prints were studied. Optimized print parameters, as well as the material's low viscosity, resulted in void-free prints that exhibited isotropic tensile properties comparable to or better than compression molded values. This work broadens the material window for FFF and demonstrates that hot melt adhesives can be used to additively manufacture optically transparent, flexible structures capable of >1200 % strain to failure. The mechanical properties of Technomelt PA 6910, combined with FFF as a versatile processing technique, make this material a candidate for a variety of applications in which transparency, design complexity, and flexibility at a wide range of temperatures are desired.

Keywords: material extrusion, fused filament fabrication, elastomers, hot melt adhesives, flexible materials, transparent parts

1. Introduction

Fused filament fabrication (FFF), a desktop form of material extrusion, is the most common additive manufacturing (AM) technique for thermoplastics. In FFF, thermoplastic filaments are heated until molten, then extruded onto a print surface layer-by-layer. Broader adoption of FFF is limited by challenges such as narrow material range, anisotropic mechanical properties, and inferior mechanical properties as compared to traditional manufacturing techniques such as injection molding or compression molding [1–5].

Acrylonitrile butadiene styrene (ABS) and polylactic acid (PLA) are the most popular polymers used in FFF due to their good printability, low cost, and mechanical properties [2,6–10]. The crystalline regimes in semicrystalline polymers enhance their strength and chemical resistance; however, increased crystallinity can also lead to more brittle materials. As a result, in conventional plastics manufacturing, processing conditions and material selection are optimized to lead to the

desired crystallinity and resulting properties for a given application. The rapid heating and cooling inherent to FFF lead to complex crystallization behavior [11,12], warpage [13,14], and poor weld strength [15,16]. Semicrystalline polymers that have been used in FFF include PLA [12,17–20], low density polyethylene (LDPE) [21], polycaprolactone (PCL) [22,23], poly(ether ether ketone) [15,24–27], poly(ethylene terephthalate),[16] caprolactam-based polyamides (commonly referred to as nylons) [28–30], polypropylene (PP) [13,14,31,32], poly(phenylene sulphide) (PPS) [11,13,33], poly(L-lactide) (PLLA)[34,35] and polybutylene succinate (PBS) [36]. In general these are plastic-grade polymers with high viscosities and rapid crystallization to different levels of ultimate crystallinity depending on cooling rate and chemical structure of the material.

Blending with amorphous polymers or compounding with reinforcements have been reported as strategies to control crystallization and warpage of prints [37–40]. For example, Spoerk et al. found that the addition of 10 vol.% short carbon fiber to PP substantially reduced warpage [40]. The same group later reported that glass microsphere-filled PPs could be optimized with greater interfacial compatibility to both reduce warpage and improve impact strength [41].

Thermoplastic elastomers (TPEs) offer high flexibility and good solvent and chemical resistance, which lead to their use in industries including automotive, footwear, medical devices, and adhesives and sealants [42]. FFF of TPEs is an emerging area of research, since AM enables part complexity and customization. TPEs typically suffer from filament buckling, although sufficiently high elastic moduli allow the filament to act as a piston, driving the melted polymer through the nozzle without buckling [5,43]. Filament buckling has also been addressed by development of pellet-fed printers [44], by use of direct feed printers that support the filament the whole path from leading rollers to the heating chamber, by making custom changes to available printers, and by cooling the filament to increase filament column stiffness [45,46]. Another challenge with printing TPEs is annular backflow, in which low viscosity melt flows backward (i.e., away from the nozzle exit) and stops the print by solidifying around the filament. Backflow can be avoided by tight control of the filament diameter and by increasing the feed rate, which enables printing in the shear thinning regime [5]. However, increased print speeds increase the filament's propensity to buckle [43]. Therefore, optimization of print speed is required to avoid buckling and annular backflow.

Similar to rigid thermoplastics, FFF-printed elastomers suffer from inferior and anisotropic mechanical properties [46,47]. Chaudhr et al. studied the effect of raster angle, layer height, and infill percentage on the mechanical performance of thermoplastic polyurethane (TPU) prints. Varying the raster angle resulted in anisotropic mechanical properties of prints and decreasing the layer height from 0.4 mm to 0.1 mm increased the tensile strength of prints by 36.5 %. Infill percentage was found to be a critical factor influencing mechanical properties of prints at high strain rates [46]. Ellson et al. studied the effect of raster angle on the mechanical strength of polythiourethan by printing 1 mm thick vertical sheets and cutting tensile bars with roads parallel (0°) and perpendicular (90°) to the applied load. Samples with 90° raster angle failed before yield with less than 10 % elongation at break, while 0° raster angle samples showed over 300 % elongation at break. These anisotropic mechanical properties are attributed to the limited mixing between layers in FFF process, which results in voids between layers [47]. Lin et al. minimized voids in FFF-printed TPU parts by modifying the layer height. However, they could not eliminate voids, which resulted in anisotropic mechanical properties. Lower layer height improved molecular diffusion and bonding strength through the squeezing effect and high pressure of the nozzle on printed roads [48].

In this study, Technomelt PA 6910, a polyamide-based semicrystalline hot melt adhesive was printed using FFF. Hot melt adhesives are solvent-free adhesives that are commonly used in bookbinding, shoe making, and other lamination applications where use of solvents is untenable. Technomelt PA 6910's sub-ambient glass transition temperature (T_g) and high melting temperature (T_m) lead to flexibility as well as high toughness and strength. This combination of properties makes it an interesting candidate for FFF. Its printability, the effect of processing on weld strength, and the effect of processing during filament fabrication and FFF printing on crystallization were investigated.

2. Materials and Methods

2.1 Materials

Technomelt PA 6910, which is a semicrystalline flexible thermoplastic, was used in this study. It was kindly provided by Henkel Corporation in the form of strand cut pellets. It is a polyamide-based hot melt adhesive.

2.2 Filament Extrusion

A Dr. Collin single screw extruder (COLLIN Lab & Pilot Solutions GmbH) was used to extrude filaments with a diameter of 2.85±0.06 mm using a 3.5 mm diameter die. The transition zone of the extruder was set to a melting temperature of 195 °C and screw speed of 20 rpm. The extruded filament was water cooled and a Davis-Standard Corporation caterpillar puller was used to adjust the filament diameter by pulling at a speed of 19.8 rpm. The tight tolerance in filament diameter is critical for achieving uniform material extrusion during FFF. Therefore, filament diameter was measured using a digital caliper every 30 seconds during extrusion to assure tight tolerance along with whole length of the three collected spools of filament.

2.3 FFF

Tensile bars and single wall hollow boxes were printed on an Ultimaker 3 with a 0.4 mm nozzle diameter in a laboratory with temperature controlled at 22 ± 1 °C. One set of tensile bars were printed at home on the same printer under less controlled temperature conditions (18-23 °C), which offered an opportunity to investigate the effect of printing environment on tensile properties. Cura 4.3, an open source slicer, was used to generate G-code. Tensile bars were printed with samples oriented in the XY plane, meaning that the largest surface area plane of the specimen was in contact with the print bed. The print bed temperature was set to 60 °C for all prints. Since this is the first report of FFF of hot melt adhesives, a range of print parameters were attempted to determine the combination that provides acceptable print quality. Print parameter combinations that were investigated are summarized in Table 1. The effect of different temperatures and layer heights on mechanical performance of prints was investigated. Raster angle, which is defined as the angle between the direction of the infill roads with respect to the X-axis of the print bed, was also varied to assess its effect on printability and tensile properties. 0°, 45°, and 90° raster angles were investigated. Good quality specimens were achieved at a print speed of 30 mm/s, extruder temperature of 220 °C, layer height of 0.15 mm, and infill percentage of 110%. Additionally, 3 cm tall single wall boxes sides 10 cm in length were printed at an extruder temperature of 220 °C, print speed of 30 mm/s, and layer height of 0.15 mm. Trapezoidal prisms were also printed to assess the ability to print overhangs with 45° and 60° angles.

Table 1. Print parameters for tensile bar fabrication

Sample	Extruder Temperature (°C)	Print Speed (mm/s)	Raster angle (°)	Layer Height (mm)	Infill (%)	Printing Environment
A	220	30	0	0.15	110	Laboratory
B	220	30	45	0.15	110	Laboratory
C	220	30	90	0.15	110	Laboratory
D	160	30	90	0.15	110	Laboratory
E	180	30	90	0.15	110	Laboratory
F	200	30	90	0.15	110	Laboratory
G	240	30	90	0.15	110	Laboratory
H	220	30	90	0.06	110	Laboratory
I	220	30	90	0.30	110	Laboratory
J	180	30	0	0.15	110	Laboratory
K	220	30	0	0.15	110	Home

2.4 Rheology

Rheological characterization was conducted using both capillary and parallel plate rheometers. Capillary rheology was performed on as-received pellets at temperatures from 140 °C to 220 °C in 20 °C increments to determine the viscosity of Technomelt PA 6910 at high shear rates ranging from 1000 1/s to 7000 1/s. It was conducted on a Dynisco LCR 7000 rheometer using capillaries with 0.762 mm diameter and three different lengths. Parallel plate rheology was performed using an ARES-G2 (TA Instruments) rheometer at 220 °C with a gap size of approximately 1.35 mm, using 25 mm diameter discs. Rheological analyses were performed on three samples for each condition. However, due to the extremely good repeatability of results (no more than 0.03 % variability), only one of them was used for further analysis.

2.5 Thermal Analysis

Thermal analysis was used to determine transition temperatures and to investigate the effect of rapid cooling, such as that associated with FFF, on crystallization. Thermogravimetric analysis (TGA) was performed on as-received pellets to determine the degradation temperature of Technomelt PA 6910. TGA was conducted on two samples from as-received pellets using a Discovery TGA (TA Instruments) and samples were heated at 10 K/min to 700 °C under a nitrogen atmosphere. Differential scanning calorimetry (DSC) was performed on as-received pellets, extruded filaments, and printed specimens. The samples from printed specimens were taken from tensile bars and also from top and bottom layers of single-wall printed hollow boxes. DSC was conducted on three samples for each thermal cycle using a Discovery DSC (TA Instruments). The samples for DSC were prepared in aluminum hermetic pans. Samples were heated from -50 °C to 250 °C, cooled to -90 °C, and again heated to 250 °C with heating and cooling rates of 10 K/min.

2.6 Tensile Testing

Six ASTM D638-14 type-V tensile bars were printed for each set of parameters. Tensile testing was conducted on an Instron 4444 with a 2 kN load cell in accordance with ASTM D638-14. A crosshead speed of 75 mm/min was used so that rupture time fell within the recommended time range of 30 seconds to 5 minutes.

2.7 Scanning Electron Microscopy (SEM)

SEM was performed with a JEOL JSM 6390 (Jeol USA Inc). Cryogenic fractured cross-sections of one sample for each printing condition were imaged to investigate the welding quality between printed roads. Fracture surfaces of tensile bars were also imaged by SEM to assess fracture.

2.8 Ultraviolet/Visible (UV/Vis) spectroscopy

To evaluate transparency of the printed tensile bars, UV/Vis spectroscopy was performed on a Cary 8454 spectrophotometer. The tensile bar printed according to condition A was placed into the chamber and scanned from 200−1100 nm at 1 nm intervals. Two bars were characterized.

3. Results and Discussion

3.1 Filament Extrusion

The temperature range for filament extrusion was obtained based on TGA and DSC analysis. From TGA (Supplementary Information, Fig. SI.1), the degradation onset temperature of Technomelt PA 6910 is 420 °C. Thus, processing must be performed below 420 °C to avoid degradation of the resin. To determine the lower bound of the processing temperature range, DSC was performed on as-received pellets (Fig. 1). Two melting peaks were observed, at 68 °C and 84 °C, in the first heating cycle. Therefore, the melt processing window was determined to be between the second melting point, 84 °C, and the degradation onset temperature, 420 °C.

Die drool was observed when the metering zone temperature was set below 195 °C. Die drool occurs when shorter polymer chains or additives migrate to the die wall and is due to the increased shear stress. Die drool can increase at high or low temperatures, and optimized extrusion temperature profile is required for each material [49]. By increasing the temperature in the metering zone of the screw to 195 °C, die drool was avoided. Additionally, this higher temperature resulted in the melt being extruded in a stable state, which made it easier to control the filament diameter to 2.85 mm with tight tolerance.

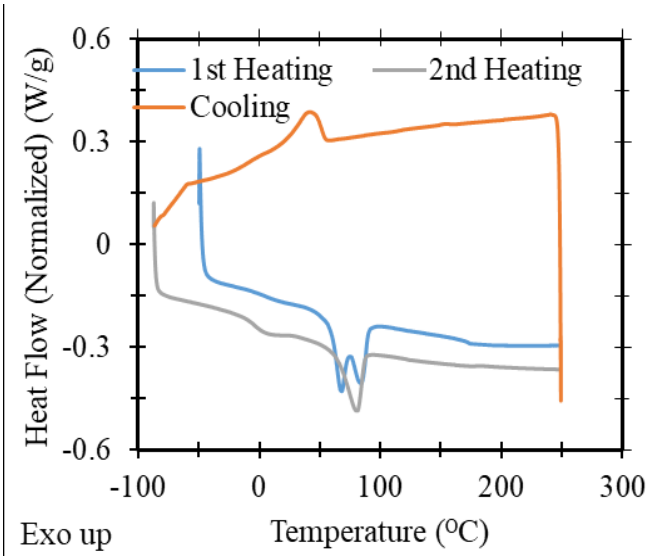

Figure 1. DSC of as-received Technomelt PA 6910 pellets.

3.2 Rheology

Results from capillary rheology of Technomelt PA 6910 at different temperatures are shown in Fig. 2. Shear-thinning was observed, as well as a decrease in the viscosity with increasing temperature, which are characteristics of thermoplastic materials. To investigate the viscosity at printing temperature, the apparent shear rate under printing condition was calculated according to Eq. 1:

$$\dot{\gamma}_{app} = \frac{4Q}{\pi r^3} \quad (1)$$

$\dot{\gamma}_{app}$ is the apparent shear rate (1/s), Q is the volumetric flow rate (mm^3/s), and r is the nozzle radius (mm). Eq. 1 assumes a Newtonian fluid, which Technomelt PA 6910 is not based on the shear-thinning shown in Fig. 2. Therefore, a power-law correction, Eq. 2, was applied to obtain corrected wall shear rate:

$$\dot{\gamma}_{wall} = \frac{1}{4}\dot{\gamma}_{app}\left[3 + \frac{1}{n}\right] \quad (2)$$

$\dot{\gamma}_{wall}$ is the corrected wall shear rate and n is the power-law index. n was calculated to be 0.64 by fitting the slope of the log complex viscosity vs. log angular frequency in the non-linear region (4 rad s^{-1} to 250 rad s^{-1}). The $\dot{\gamma}_{wall}$ was calculated as 684 s^{-1} [50].

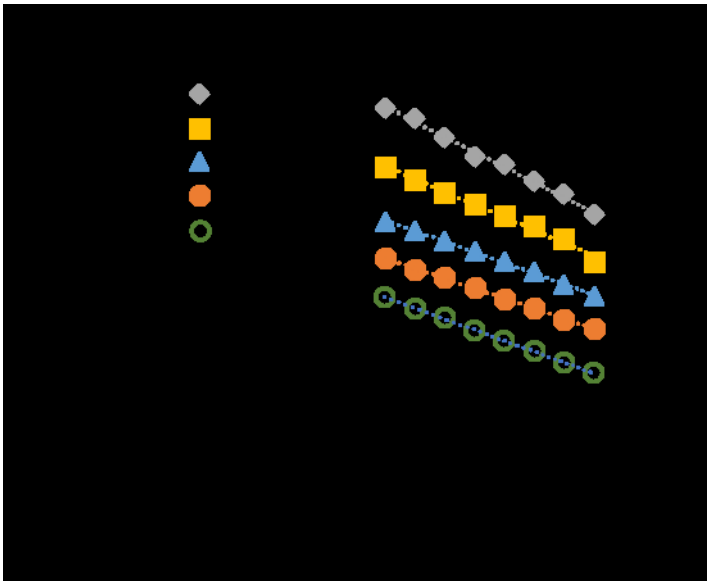

Figure 2. Capillary rheology of Technomelt PA 6910 as-received pellets at a range of FFF-relevant temperatures.

The shear viscosity of Technomelt PA 6910 feedstock at the printing condition was determined by combining the data from parallel plate and capillary rheology as shown in Fig. 3. The Bagley and Rabinowitsch corrections were applied to the shear stress and shear rate data from capillary rheology results to remove entrance effects and correct for a non-parabolic velocity profile, respectively. From Fig. 3, alignment is seen between corrected capillary rheology data and parallel plate rheology data as suggested by the Cox-Merz relationship [51]. The viscosity of Technomelt PA 6910 at the calculated wall shear rate of 684 s^{-1} is estimated to be 45 Pa·s, which is notably lower than other printable thermoplastics at similar shear rates. The viscosities of a number of

ABS grades at 240 °C and 684 s^{-1} range from 110 to 130 Pa·s, while viscosities for commercially available TPUs range from 90 to 110 Pa·s at 220 °C and the same shear rate [52].

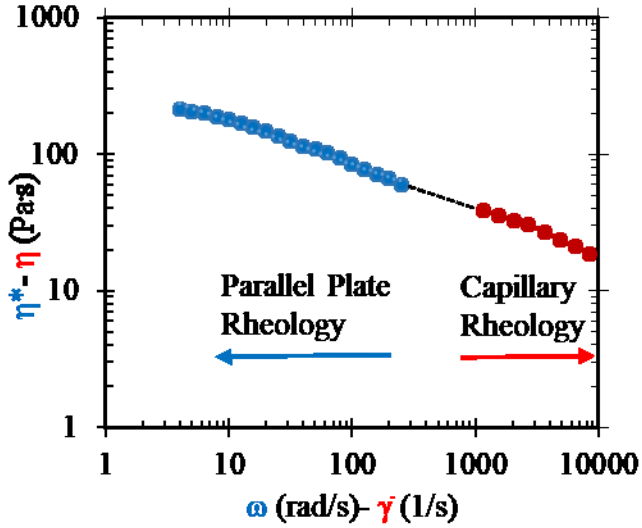

Figure 3. Rheological behavior of Technomelt PA 6910 at a temperature of 220 °C.

3.3 FFF

A print speed of 30 mm/s was used for FFF because the Technomelt PA 6910 filament is flexible and, therefore, prone to buckling while passing through the feeding system gear at higher print speeds. At higher print speeds, buckling of the filament decreased the extrusion rate of the melt from the nozzle, or even stopped extrusion and caused print failure. No shrinkage or warpage was observed in printed structures, which is attributed to the slow crystallization, and strong adhesion of the first layer of printed material to the glass build plate, respectively.

The effect of extrusion temperature on print quality was investigated by printing tensile bars at a range of temperatures (160 °C-240 °C, sample conditions C, D, E, F, and G from Table 1). Images of these samples are provided in Fig. 4. The tensile bars printed at 160 °C-200 °C exhibited poor weld quality and interlayer adhesion, which resulted in opaque prints as shown in Fig. 5a. The poor weld quality at low temperatures is due to the failure of the hot end to melt and extrude material through the nozzle at the rates required for a print speed of 30 mm/s. By increasing the temperature to 220 °C and 240 °C, improved interlayer adhesion was observed, which resulted in transparent samples as seen in Fig. 5b. At an extruder temperature of 240 °C, in spite of good interlayer welding, flash was observed on the bar edges due to the over extrusion caused by shear thinning and reduced viscosity of the extruded material. Since the flash was seen in initial layers, it seems that this low viscosity melt that was printed in contact with the heated print bed was not able to cool down fast enough to retain its shape. Based on these results, an extruder temperature of 220 °C was selected as the default for further investigation. The effect of layer height (0.06 mm, 0.15 mm, and 0.3 mm), raster angle (0^O, 45^O, and 90^O), and room temperature on print quality was also investigated by printing tensile bars with the sample conditions of A, B, C, H, I and K from Table 1.

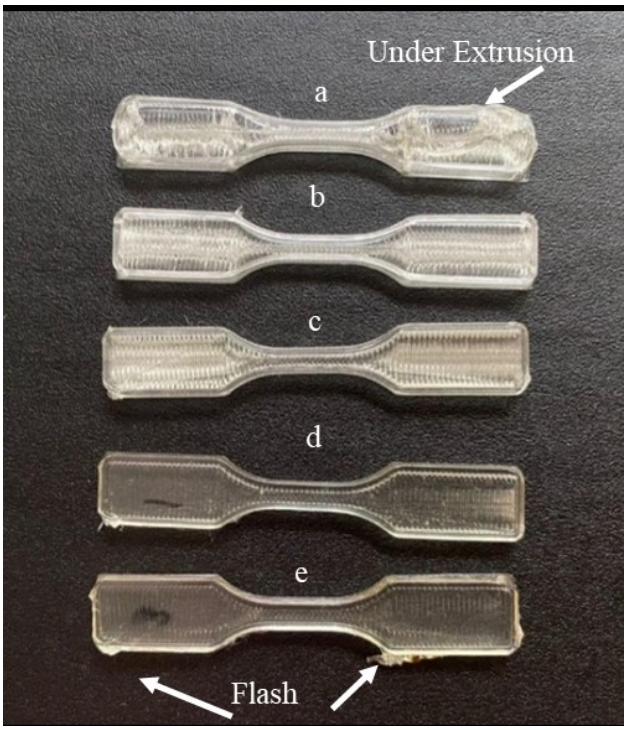

Figure 4. Tensile bars printed at different extruder temperatures: a. 160 °C; b. 180 °C; c. 200 °C; d. 220 °C; e. 240 °C, sample conditions of C, D, E, F, and G from Table 1.

Figure 5. Effect of extruder temperature on transparency of samples printed at a. 180 °C (sample condition A); b. 220 °C (sample condition J).

Technomelt PA 6910 can be printed in more complicated geometries with large overhangs, as shown in Fig. 6a. It was printed at 220 °C with a print speed of 30 mm/s and a layer height of 0.15 mm. Additionally, the printed structures are highly flexible, as shown in Fig. 6b.

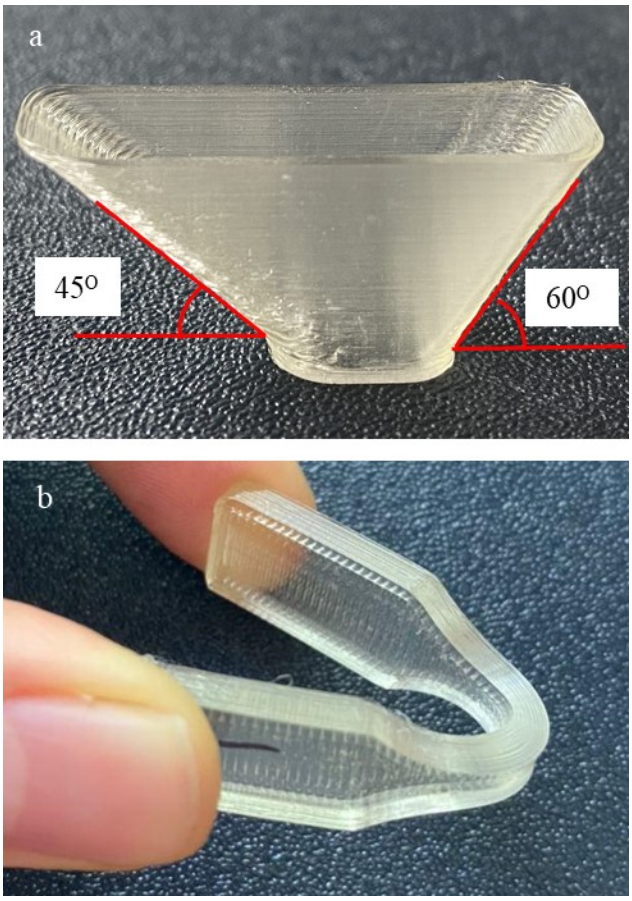

Figure 6. a. FFF printed trapezoidal prism with the 45° and 60° overhangs; b. Tensile bar (sample condition C) exhibiting high flexibility.

UV/Vis spectroscopy was performed on the tensile bar shown in Fig. 5b to evaluate its transparency. The results (shown in Fig. SI.2) give 12-16 % transmittance in the range of visible light (400 to 700 nm). The light transmission through the 3.5 mm thick tensile bar is higher than that through 0.4 mm thick walls printed using clear PLA, and HD Glass [53]. However, the light transmittance is lower than expected based on Fig. 5b. We attribute the lower than expected transmittance to light scattering from the rough surface of the printed tensile bar as a result of the layer lines. Therefore, coating the surface with a transparent resin [53] and/or polishing the rough surface would be expected to improve light transmission through the prints [54].

3.4 Tensile Testing

The results from tensile testing of printed bars at different raster angles can be seen in Fig. 7 and Fig. 8. All samples yield around 50 % strain. Parts with 0°, 45°, and 90° raster angles exhibit similar behavior, with no statistically significant differences in yield strain (ε_y), yield strength (σ_y), and ultimate tensile strength (σ_f) at a 95% confidence interval (one-way analysis of variance, $p < 0.05$). Elongation at break (ε_f) is statistically significantly lower in parts with 0° raster angle ($p < 0.05$), but the results are all still within 1,104 – 1,265 % strain. The observed isotropic tensile properties of FFF prints are unexpected, since the highest mechanical properties typically occur in prints with a 0° raster angle because loading occurs along the length of printed roads in this print

orientation [2,8,17,55–57]. The isotropic mechanical properties of prints indicate excellent bonding between roads.

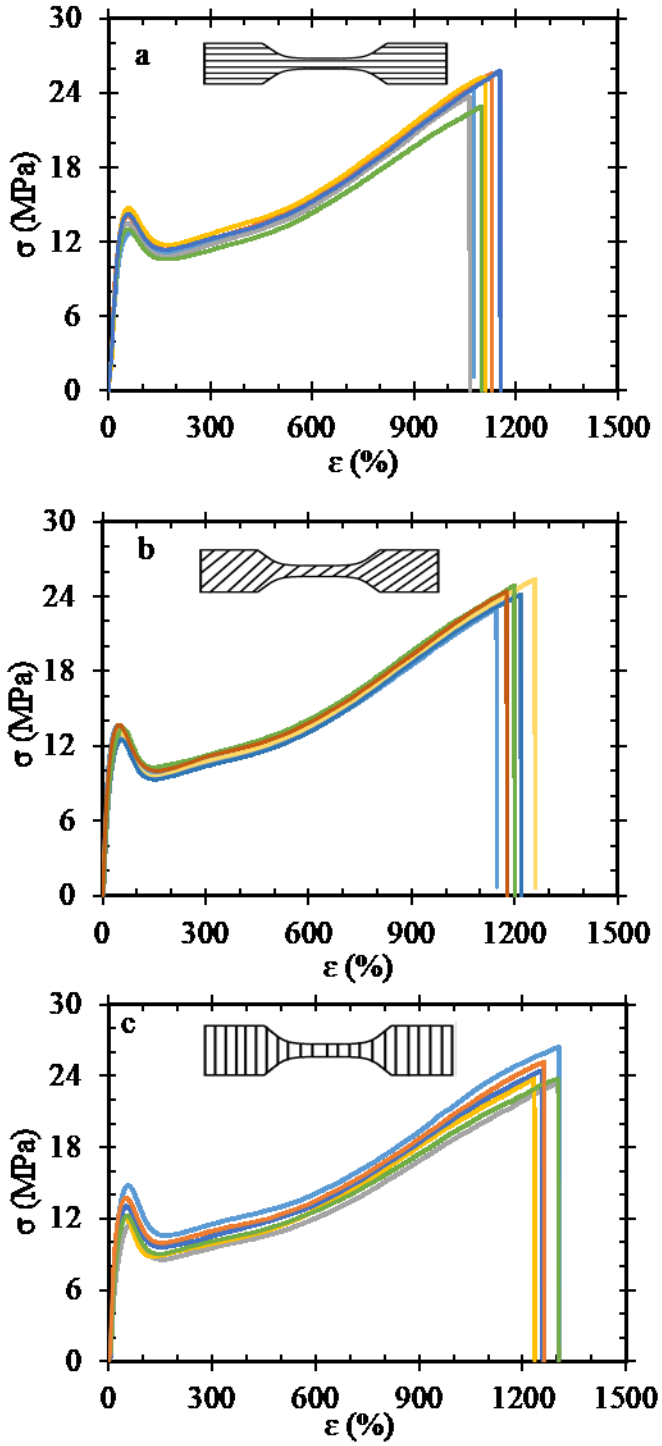

Figure 7. Tensile testing results of samples A, B, and C from Table 1. a. 0°; b. 45°; c. 90° raster angle.

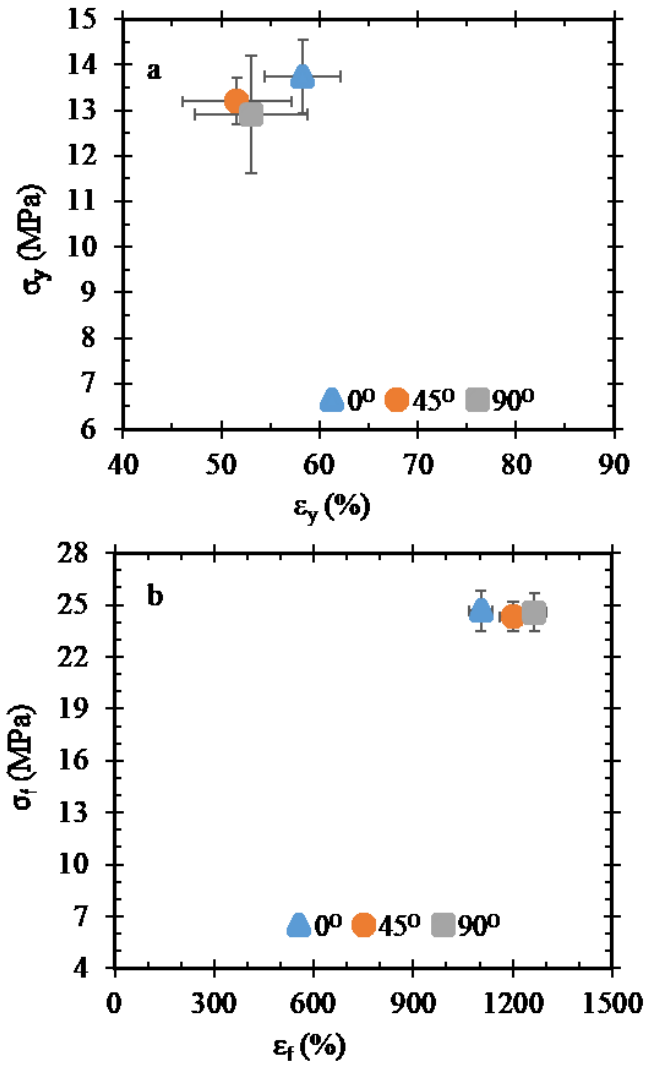

Figure 7. Tensile analysis of samples printed with different raster angles. a: Yield strength versus yield strain, b: Ultimate tensile strength versus strain to failure. Error bars represent 95 % confidence intervals.

Some samples with a 0° raster angle were printed at home under a less controlled temperature and humidity environment (sample condition K). Tensile testing results are shown in Fig. 9. Printing at home resulted in a 10% decrease in σ_y and significant fluctuations in σ_f and ε_f. These differences are likely due to different cooling rates and minimum temperatures during printing of the part due to variations in the room temperature during printing, which can alter crystallization. To minimize possible effects of humidity, filament and printed parts were stored in sealed containers except for during print. This approach was deemed successful based on an absence of bubbles or foaming observed during printing.

As roads are extruded during FFF, they experience high shear stresses that can cause stretching and orienting of polymer chains in the print direction [58]. Crystalline regimes primarily contribute to the pre-yield mechanical properties, while amorphous regimes contribute more to the post-yield

strength. Therefore, differences in tensile properties for samples printed at home can result from differences in crystallization kinetics.

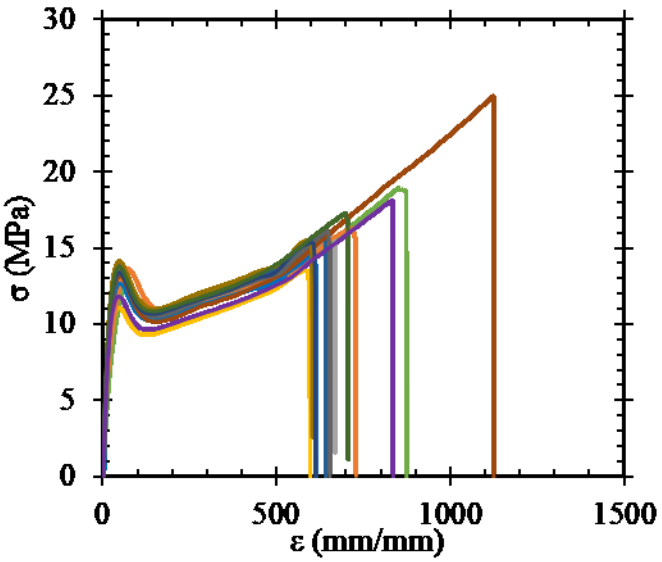

Figure 9. Tensile testing results of samples with 0° raster angle printed at home (printing condition K from Table 1).

Indeed, samples printed in a laboratory environment with controlled temperature exhibit an melt enthalpy that is 10.8 % higher than in 0° prints (Supplementary Information, Fig. SI.3). From these results, the lower yield strength for printing condition K may be attributed to the faster cooling due to the lower environment temperature, which results in faster cooling to temperatures below crystallization temperature and lower crystallization. Lower percent crystallinity decreases the yield strength and possibly also ultimate tensile strength [59]. The large effect of room temperature on crystallization of Technomelt PA 6910 is likely due to its sub-ambient T_g and low T_m, which suggests that crystallization at room temperature plays a significant role in the final crystalline content of prints. Motivated by these findings, ongoing efforts by the authors include in-depth characterization of Technomelt PA 6910's crystallization kinetics.

Results from tensile testing of specimens printed at a range of temperatures are shown in Fig. 10. By increasing the temperature from 180 °C to 220 °C, yield strength and tensile strength of the printed parts improved. However, tensile bars printed at 220 °C exhibit statistically significantly higher ultimake tensile strength as compared to bars printed at 240 °C ($p < 0.05$). Specimens printed at 240 °C exhibited similar enthalpy of crystallization to 220 °C prints (Supplementary Information, Fig. SI.3). These results indicate that percent crystallinity is not the source of lower mechanical properties at 240 °C. It is unlikely that the differences in tensile properties are due to degradation given Technomelt PA 6910's decomposition temperature of 420 °C. Possible reasons include differences in where crystalline regimes form at the two extrusion temperatures and differences in chain alignment. The first possible explanation is being explored in ongoing modeling work.

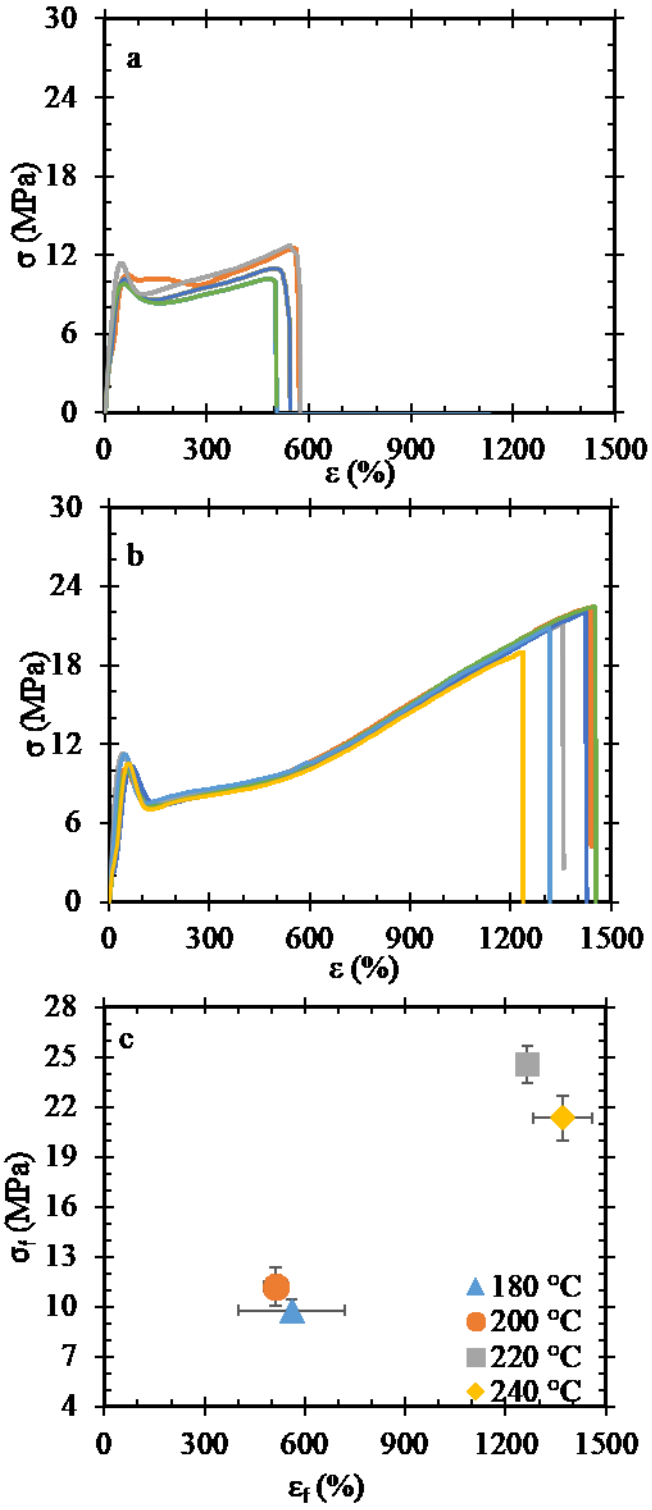

Figure 10. Stress-strain curves for tensile bars printed at extrusion temperatures a. 200 °C; b. 240 °C. c. Tensile properties of samples printed at a range of extrusion temperatures (sample conditions C, E, F, and G). Error bars represent 95 % confidence intervals.

The effect of layer height on tensile properties can be seen in Fig. 11. Samples printed with a layer height of 0.15 mm exhibit the highest tensile properties, while the samples with a layer height of 0.06 mm exhibit the lowest mechanical properties. The lower layer height reduces to amount of contact between adjacent roads in the X-Y plane, which may explain this drop in properties. Conversely, the lower nozzle pressure associated with the higher layer height of 0.3 mm may be the reason for lower properties than the 0.15 mm condition. The small error bars in tensile properties of samples with the layer height of 0.3 mm, implies that the applied pressure at lower layer heights is the possible source of higher variability in tensile properties at lower layer heights.

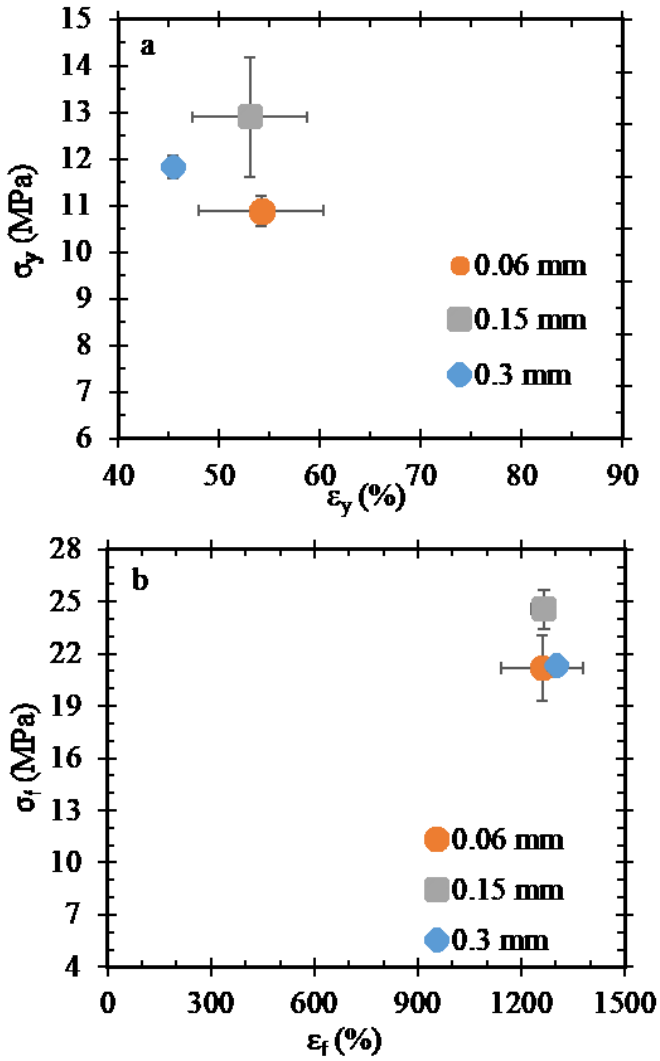

Figure 8. Tensile properties of specimens with different layer heights (sample conditions C, H, and I). a. Yield strength versus yield strain; b. Ultimate tensile strength versus strain to failure. Error bars represent 95 % confidence intervals.

Overall, the mechanical properties do not change a large amount for layer heights ranging from 0.06 mm to 0.3 mm. It can be concluded that extrusion temperature plays the most important role in the printed properties of this material. The low viscosity of this material at high temperatures

improves interlayer adhesion, which overwhelms any effect of pressure change as a result of layer height variation.

The yield strength and ultimate tensile strength of compression molded samples are reported by the supplier as 11 MPa and 26 MPa, respectively, which are comparable with printed samples at different raster angles and an extruder temperature of 220 °C.

Cryogenically fractured cross-sections of FFF tensile bars printed at 220 °C with different raster angles are shown in Fig. 12 a, c, and e. No voids are apparent between deposited roads, which is unusual for FFF parts. Good consolidation between roads is observed and printed roads are not distinguishable, which is likely due to Technomelt PA 6910's low viscosity under print conditions. Fracture surfaces of the samples with different raster angles from tensile tests are shown in Fig. 12 b, d, and f. All three raster angle fracture surfaces show crack propagation across multiple layers, which contributes to increased strength and toughness. The presence of fibrils on the fracture surface and path change during fracture between different layers indicate a high amount of plastic deformation before failure, which results in ductile fracture. The cryogenically fractured cross-section and tensile surface of a FFF tensile bar printed at home are shown in Fig. 13 a and b. The folding next to the fracture paths in the tensile fractured cross-section of the sample indicates substantial elastic deformation before failure and lower toughness of the part. However, multiple narrow fracture paths suggest some extent of plastic deformation as well [60,61]. The lower toughness of parts printed at home can be due to the lower crystallization of the parts. For all parts, fracture surfaces are void-free and the boundaries between roads in a single layer cannot be distinguished, which is consistent with their isotropic tensile properties. This feature is rare, with most reports of fracture surfaces from FFF structures exhibiting visible voids and non-consolidated roads within a layer [62–64]. Previous work has demonstrated that voids between roads can be minimized by changing the infill percentage in different layers [65]. The absence of voids between adjacent beads in this study leads to a high density/high solidity ratio [66], which facilitates high mechanical properties and comparable ultimate tensile strength and yield strength with compression molded parts. Additionally, void-free cross-sections indicate that the differences in void fractions are likely not the cause of the fluctuation in mechanical properties in home-printed samples seen in Fig. 9.

The absence of voids is attributed to the optimized print parameters as well as the low viscosity of Technomelt PA 6910 under print conditions. Technomelt PA 6910's low viscosity allows for high inter- and intra-layer polymer diffusion. Optimal printing conditions include an extruder temperature 136 K above T_m (185 K above the crystallization temperature, T_C), which extends the time between road deposition and solidification.

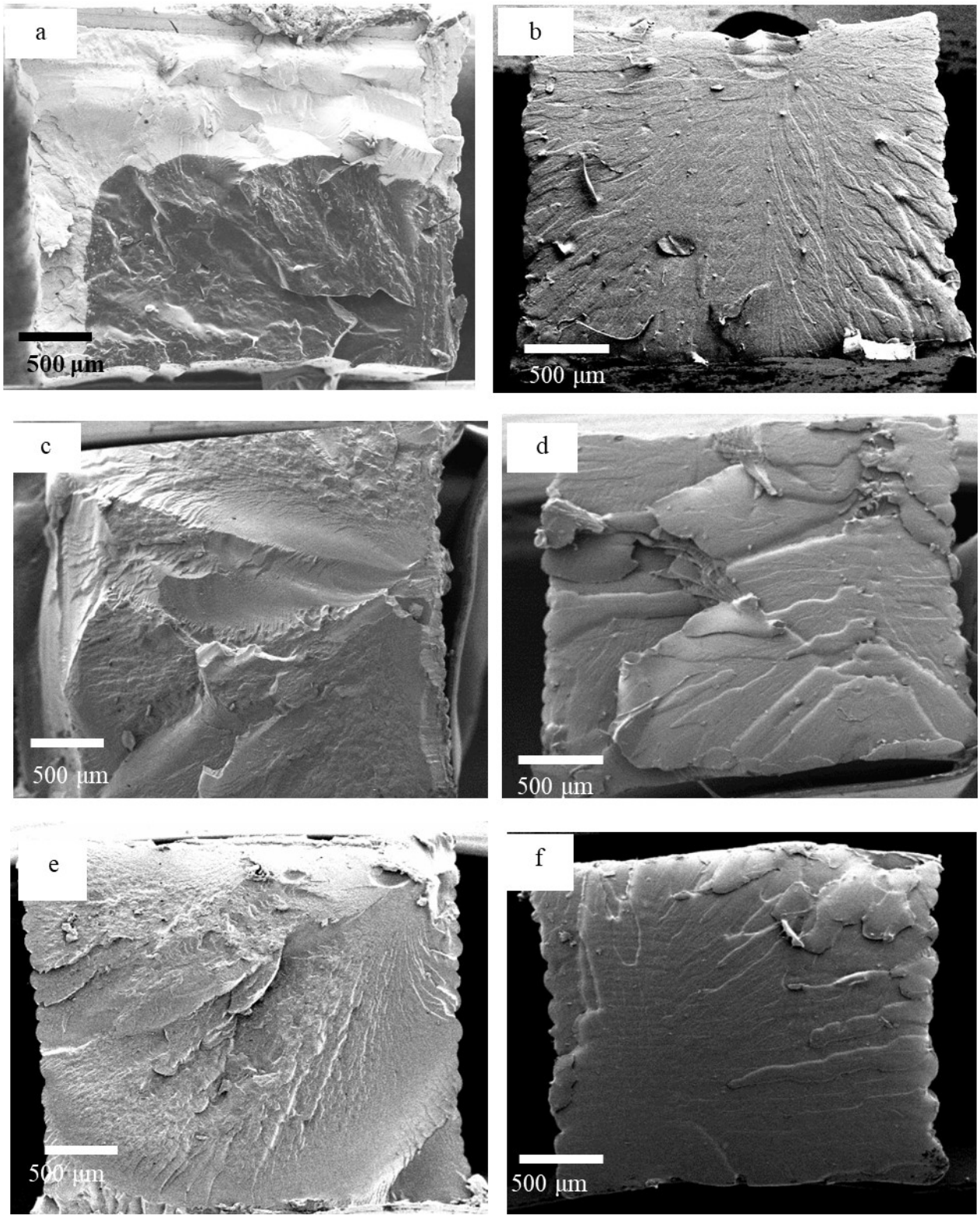

Figure 9. SEM images from cryogenic fracture surfaces (a, c, e) and tensile fracture surfaces (b, d, e) of samples A, B, and C from Table 1. a,b. 0°; c,d. 45°; e,f. 90° raster angles. Images show a y-z plane of the tensile bars.

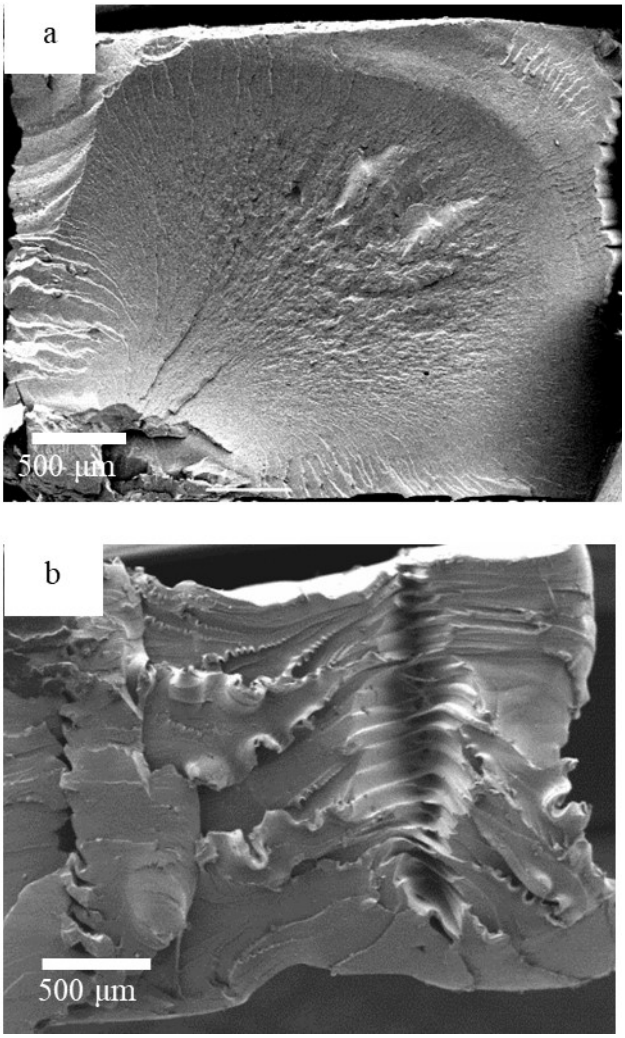

Figure 10. SEM images from cryogenic fracture surface (a) and tensile fracture surface (b) of sample K from Table 1. These specimens were printed at home with 0° raster angle. Images show a y-z plane of the tensile bars.

3.5. DSC

Results from DSC of as-received pellets, filament, and different sections of printed parts are shown in Fig. 14. Two melting peaks are observed around 68 °C and 84 °C, indicating two distinct crystalline morphologies. The first peak is most distinct in as-received pellets. In pellet processing, shear-induced crystallization occurs in the skin of strands, and the relatively larger size of the first peak in the as-received pellets suggests that the cooling rate was slow enough or the annealing time was long enough to promote crystal growth. In the second heating cycle of pellets, thermal history from processing is removed and there are no signs of the first melting peak. In filament processing, the fast cooling rate (water-cooled) suppresses the growth of shear-induced spherulites, and therefore, the first melting peak shrinks. The second peak widens due to the slower cooling in the filament core and growth of crystallites. Printed structures exhibit a negligible first melting peak, which is desirable in terms of higher service temperature. An explanation for this phenomenon is that shear-induced crystallization is a secondary crystallization mechanism in FFF

because high print temperatures enable relaxation of extrusion-oriented polymer roads before reaching T_c [67].

The enthalpy of melting as shown in Fig. 14b is highest in the first heating cycle of pellets, which is due to the shear stresses applied during processing, the thermal history of pellet processing, and long annealing time (some weeks) at room temperature before testing. Due to the short annealing time and no shearing, the enthalpy of fusion is lower in the second heating cycle of pellets. In the bottom layers of printed samples, the cooling rate is slower due to the proximity to the heated print bed or additional thermal mass [68], which facilitates annealing at higher temperatures. For the cube bottom, the amount of crystallinity returns to the level of as-received pellets. The transparency and high flexibility of printed structures indicate that crystallites are sufficiently small to allow light transmission, which leads to transparency while maintaining mechanical properties that are comparable to compression molded samples.

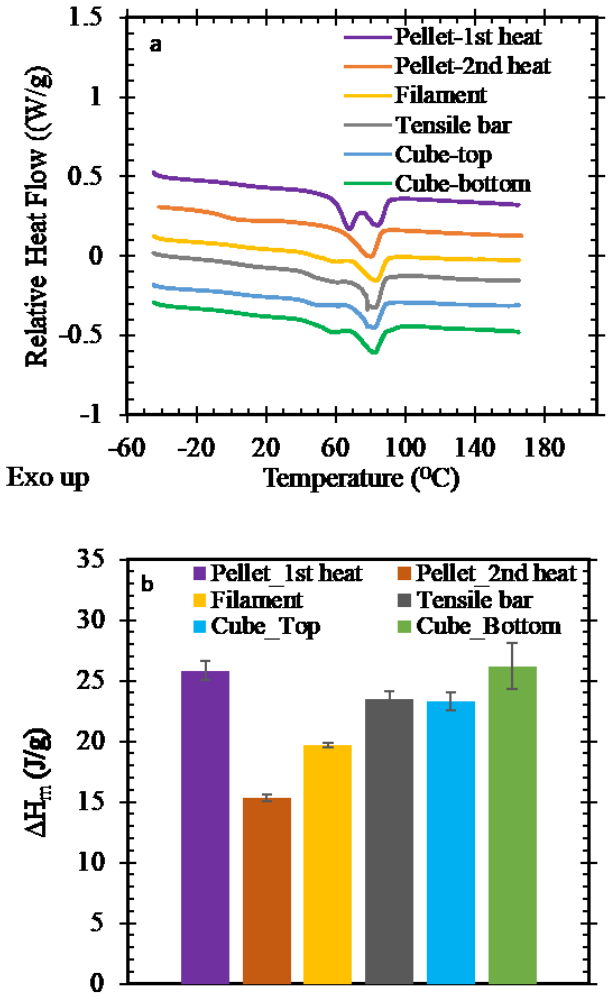

Figure 11. a. DSC of Technomelt PA 6910 after different processing conditions. Graphs are shifted vertically; b. Melt enthalphy results from DSC of Technomelt PA 6910 after different types of processing. n = 3 and error bars represent 95 % confidence intervals.

4. Conclusions

Optimizing print parameters to take advantage of hot melt adhesives' low viscosities, slow crystallization, and high melt strengths have been shown to be an effective means for improving the mechanical properties of printed parts and eliminating voids within prints. An extruder temperature of 220 °C resulted in smooth printing of roads at a print speed of 30 mm/s.

While dependence of tensile properties on raster angle is well-established, Technomelt PA 6910 exhibited isotropic tensile properties in prints with the raster angles of 0°, 45°, and 90°. Ambient temperature was observed to affect percent crystallinity and tensile properties of Technomelt 6910 prints, due to this material's sub-ambient T_g, which facilitates crystallization at room temperature. The parts printed at raster angles of 0°, 45°, and 90° with an extrusion temperature of 220 °C exhibited ultimate tensile strengths comparable with compression molded parts. The effect of layer height on mechanical properties of printed structures is not significant because excellent coalesence is achieved at the extrusion temperatuer used for all layer heights. At all raster angles, elongations were very high – more than 520 % – and above that reported for compression molded samples of the same material (~500 %). The recovery of crystallinity during printing to that of the as-received material is likely a contributing factor in achieving mechanical properties comparable to bulk. Combined, this work broadens the material window for FFF and demonstrates that hot melt adhesives can be used to additively manufacture optically transparent, flexible structures capable of >1200 % strain to failure with isotropic tensile properties.

Conflicts of interest

The authors declare that they have no known competing financial interests or personal relationships that could have appeared to influence the work reported in this paper.

Acknowledgements

The authors acknowledge financial support from the National Science Foundation (CMMI-1853480). The authors also thank the Henkel Corporation for providing Technomelt PA 6910 and Charles Paul, Luca Marchese, and Tim Welters of the Henkel Corporation for insightful conversations and guidance.

References

[1] S.H. Ahn, M. Montero, D. Odell, S. Roundy, P.K. Wright, Anisotropic material properties of fused deposition modeling ABS, Rapid Prototyp. J. (2002). https://doi.org/10.1108/13552540210441166.

[2] A.M. Peterson, Review of acrylonitrile butadiene styrene in fused filament fabrication: A plastics engineering-focused perspective, Addit. Manuf. 27 (2019) 363–371. https://doi.org/10.1016/j.addma.2019.03.030.

[3] J.J. Laureto, J.M. Pearce, Anisotropic mechanical property variance between ASTM D638-14 type i and type iv fused filament fabricated specimens, Polym. Test. (2018).

https://doi.org/10.1016/j.polymertesting.2018.04.029.

[4] J.R.C. Dizon, A.H. Espera, Q. Chen, R.C. Advincula, Mechanical characterization of 3D-printed polymers, Addit. Manuf. 20 (2018) 44–67. https://doi.org/10.1016/j.addma.2017.12.002.

[5] E.L. Gilmer, D. Miller, C.A. Chatham, C. Zawaski, J.J. Fallon, A. Pekkanen, T.E. Long, C.B. Williams, M.J. Bortner, Model analysis of feedstock behavior in fused filament fabrication: Enabling rapid materials screening, Polymer (Guildf). (2018). https://doi.org/10.1016/j.polymer.2017.11.068.

[6] S. Bakrani Balani, F. Chabert, V. Nassiet, A. Cantarel, Influence of printing parameters on the stability of deposited beads in fused filament fabrication of poly(lactic) acid, Addit. Manuf. (2019). https://doi.org/10.1016/j.addma.2018.10.012.

[7] A.C. Abbott, G.P. Tandon, R.L. Bradford, H. Koerner, J.W. Baur, Process-structure-property effects on ABS bond strength in fused filament fabrication, Addit. Manuf. (2018). https://doi.org/10.1016/j.addma.2017.11.002.

[8] J. Kiendl, C. Gao, Controlling toughness and strength of FDM 3D-printed PLA components through the raster layup, Compos. Part B Eng. 180 (2020) 107562. https://doi.org/10.1016/j.compositesb.2019.107562.

[9] A.A. D'Amico, A. Debaie, A.M. Peterson, Effect of layer thickness on irreversible thermal expansion and interlayer strength in fused deposition modeling, Rapid Prototyp. J. (2017). https://doi.org/10.1108/RPJ-05-2016-0077.

[10] M. Domingo-Espin, J.M. Puigoriol-Forcada, A.A. Garcia-Granada, J. Llumà, S. Borros, G. Reyes, Mechanical property characterization and simulation of fused deposition modeling Polycarbonate parts, Mater. Des. (2015). https://doi.org/10.1016/j.matdes.2015.06.074.

[11] E.R. Fitzharris, D.W. Rosen, M.L. Shofner, Fast scanning calorimetry for semicrystalline polymers in fused deposition modeling, Polymer (Guildf). (2019). https://doi.org/10.1016/j.polymer.2019.01.083.

[12] L. Wang, W.M. Gramlich, D.J. Gardner, Improving the impact strength of Poly(lactic acid) (PLA) in fused layer modeling (FLM), Polymer (Guildf). (2017). https://doi.org/10.1016/j.polymer.2017.03.011.

[13] E.R. Fitzharris, N. Watanabe, D.W. Rosen, M.L. Shofner, Effects of material properties on warpage in fused deposition modeling parts, Int. J. Adv. Manuf. Technol. (2018). https://doi.org/10.1007/s00170-017-1340-8.

[14] O.S. Carneiro, A.F. Silva, R. Gomes, Fused deposition modeling with polypropylene, Mater. Des. 83 (2015) 768–776. https://doi.org/10.1016/j.matdes.2015.06.053.

[15] C. Yang, X. Tian, D. Li, Y. Cao, F. Zhao, C. Shi, Influence of thermal processing conditions in 3D printing on the crystallinity and mechanical properties of PEEK material, J. Mater. Process. Tech. 248 (2017) 1–7. https://doi.org/10.1016/j.jmatprotec.2017.04.027.

[16] N.E. Zander, M. Gillan, R.H. Lambeth, Recycled polyethylene terephthalate as a new FFF feedstock material, Addit. Manuf. 21 (2018) 174–182. https://doi.org/10.1016/j.addma.2018.03.007.

[17] S.R. Rajpurohit, H.K. Dave, Analysis of tensile strength of a fused filament fabricated PLA part using an open-source 3D printer, Int. J. Adv. Manuf. Technol. 101 (2019) 1525–1536. https://doi.org/10.1007/s00170-018-3047-x.

[18] B.M. Tymrak, M. Kreiger, J.M. Pearce, Mechanical properties of components fabricated with open-source 3-D printers under realistic environmental conditions, Mater. Des. 58 (2014) 242–246. https://doi.org/10.1016/j.matdes.2014.02.038.

[19] J.M. Chacón, M.A. Caminero, E. García-Plaza, P.J. Núñez, Additive manufacturing of PLA structures using fused deposition modelling: Effect of process parameters on mechanical properties and their optimal selection, Mater. Des. 124 (2017) 143–157. https://doi.org/10.1016/j.matdes.2017.03.065.

[20] P. Ravi, P.S. Shiakolas, T.R. Welch, Poly-l-lactic acid: Pellets to fiber to fused filament fabricated scaffolds, and scaffold weight loss study, Addit. Manuf. 16 (2017) 167–176. https://doi.org/10.1016/j.addma.2017.06.002.

[21] K.R. Hart, J.B. Frketic, J.R. Brown, Recycling meal-ready-to-eat (MRE) pouches into polymer fi lament for material extrusion additive manufacturing, Addit. Manuf. 21 (2018) 536–543. https://doi.org/10.1016/j.addma.2018.04.011.

[22] R. De Santis, A. Gloria, T. Russo, A. Ronca, U. D'Amora, D. Ronca, L. Ambrosio, Viscoelastic properties of rapid prototyped magnetic nanocomposite scaffolds for osteochondral tissue regeneration, Procedia CIRP. 49 (2016) 76–82. https://doi.org/10.1016/j.procir.2015.07.037.

[23] M. Mohseni, D.W. Hutmacher, N.J. Castro, Independent evaluation of medical-grade bioresorbable filaments for fused deposition modelling/fused filament fabrication of tissue engineered constructs, Polymers (Basel). 10 (2018) 40. https://doi.org/10.3390/polym10010040.

[24] W. Wu, P. Geng, G. Li, D. Zhao, H. Zhang, J. Zhao, Influence of Layer Thickness and Raster Angle on the Mechanical Properties of 3D-Printed PEEK and a Comparative Mechanical Study between PEEK and ABS, Materials (Basel). 8 (2015) 5834–5846. https://doi.org/10.3390/ma8095271.

[25] B. Valentan, Ž. Kadivnik, T. Brajlih, A. Anderson, I. Drstvenšek, Processing poly(ether etherketone) on a 3D printer for thermoplastic modelling, Mater. Tehnol. 47 (2013) 715–721.

[26] M. Vaezi, S. Yang, Extrusion-based additive manufacturing of PEEK for biomedical applications, Virtual Phys. Prototyp. 10 (2015) 123–135. https://doi.org/10.1080/17452759.2015.1097053.

[27] S. Berretta, R. Davies, Y.T. Shyng, Y. Wang, O. Ghita, Fused Deposition Modelling of

high temperature polymers: Exploring CNT PEEK composites, Polym. Test. 63 (2017) 251–262. https://doi.org/10.1016/j.polymertesting.2017.08.024.

[28] N.G. Tanikella, B. Wittbrodt, J.M. Pearce, Tensile strength of commercial polymer materials for fused filament fabrication 3D printing, Addit. Manuf. 15 (2017) 40–47. https://doi.org/10.1016/j.addma.2017.03.005.

[29] H. Li, S. Zhang, Z. Yi, J. Li, A. Sun, J. Guo, G. Xu, Bonding quality and fracture analysis of polyamide 12 parts fabricated by fused deposition modeling, Rapid Prototyp. J. 23 (2017) 973–982. https://doi.org/10.1108/RPJ-03-2016-0033.

[30] A.N. Dickson, J.N. Barry, K.A. McDonnell, D.P. Dowling, Fabrication of continuous carbon, glass and Kevlar fibre reinforced polymer composites using additive manufacturing, Addit. Manuf. 16 (2017) 146–152. https://doi.org/10.1016/j.addma.2017.06.004.

[31] N. Bachhar, A. Gudadhe, A. Kumar, P. Andrade, G. Kumaraswamy, 3D printing of semicrystalline polypropylene: towards eliminating warpage of printed objects, Bull. Mater. Sci. (2020). https://doi.org/10.1007/s12034-020-02097-4.

[32] L. Wang, D.J. Gardner, Effect of fused layer modeling (FLM) processing parameters on impact strength of cellular polypropylene, Polymer (Guildf). 113 (2017) 74–80. https://doi.org/10.1016/j.polymer.2017.02.055.

[33] V. Kishore, X. Chen, C. Ajinjeru, A.A. Hassen, J. Lindahl, J. Failla, V. Kunc, C. Duty, Additive manufacturing of high performance semicrystalline thermoplastics and their composites, in: Proc. 27th Annu. Int. Solid Free. Fabr. Symp., 2016: pp. 906–915.

[34] A. Ahlinder, T. Fuoco, Á. Morales-López, M.A. Yassin, K. Mustafa, A. Finne-Wistrand, Nondegradative additive manufacturing of medical grade copolyesters of high molecular weight and with varied elastic response, J. Appl. Polym. Sci. (2020). https://doi.org/10.1002/app.48550.

[35] J. Marchewka, J. Laska, Processing of poly-l-lactide and poly(l-lactide-co-trimethylene carbonate) blends by fused filament fabrication and fused granulate fabrication using RepRap 3D printer, Int. J. Adv. Manuf. Technol. (2020). https://doi.org/10.1007/s00170-020-04981-z.

[36] M.V. Candal, I. Calafel, N. Aranburu, M. Fernández, G. Gerrica-Echevarria, A. Santamaría, A.J. Müller, Thermo-rheological effects on successful 3D printing of biodegradable polyesters, Addit. Manuf. (2020). https://doi.org/10.1016/j.addma.2020.101408.

[37] M. Jin, C. Neuber, H.W. Schmidt, Tailoring polypropylene for extrusion-based additive manufacturing, Addit. Manuf. 33 (2020) 101101. https://doi.org/10.1016/j.addma.2020.101101.

[38] M. Spoerk, C. Savandaiah, F. Arbeiter, J. Sapkota, C. Holzer, Optimization of mechanical properties of glass-spheres-filled polypropylene composites for extrusion-based additive

manufacturing, Polym. Compos. (2019). https://doi.org/10.1002/pc.24701.

[39] B. Brenken, E. Barocio, A. Favaloro, V. Kunc, R.B. Pipes, Fused filament fabrication of fiber-reinforced polymers: A review, Addit. Manuf. 21 (2018) 1–16. https://doi.org/10.1016/j.addma.2018.01.002.

[40] M. Spoerk, C. Savandaiah, F. Arbeiter, G. Traxler, L. Cardon, Anisotropic properties of oriented short carbon fibre filled polypropylene parts fabricated by extrusion-based additive manufacturing, Compos. Part A. 113 (2018) 95–104. https://doi.org/10.1016/j.compositesa.2018.06.018.

[41] M. Spoerk, F. Arbeiter, I. Raguž, G. Weingrill, T. Fischinger, G. Traxler, S. Schuschnigg, L. Cardon, C. Holzer, Polypropylene Filled With Glass Spheres in Extrusion-Based Additive Manufacturing: Effect of Filler Size and Printing Chamber Temperature, Macromol. Mater. Eng. (2018). https://doi.org/10.1002/mame.201800179.

[42] J.G. Drobny, Handbook of Thermoplastic Elastomers: Second Edition, 2014. https://doi.org/10.1016/C2013-0-00140-5.

[43] J. Herzberger, J.M. Sirrine, C.B. Williams, T.E. Long, Polymer Design for 3D Printing Elastomers: Recent Advances in Structure, Properties, and Printing, Prog. Polym. Sci. (2019). https://doi.org/10.1016/j.progpolymsci.2019.101144.

[44] N. Kumar, P.K. Jain, P. Tandon, P.M. Pandey, 3D printing of flexible parts using eva material, in: Mater. Phys. Mech., 2018. https://doi.org/10.18720/MPM.3722018-3.

[45] K. Elkins, H. Nordby, C. Janak, R.W. Gray, J.H. Bohn, D.G. Baird, Soft elastomers for fused deposition modeling, Solid Free. Fabr. Proceedings, Sept. 1997. (1997).

[46] M.S. Chaudhry, A. Czekanski, Evaluating FDM process parameter sensitive mechanical performance of elastomers at various strain rates of loading, Materials (Basel). (2020). https://doi.org/10.3390/ma13143202.

[47] G. Ellson, X. Carrier, J. Walton, S.F. Mahmood, K. Yang, J. Salazar, W.E. Voit, Tough thiourethane thermoplastics for fused filament fabrication, J. Appl. Polym. Sci. (2018). https://doi.org/10.1002/app.45574.

[48] X. Lin, P. Coates, M. Hebda, R. Wang, Y. Lu, L. Zhang, Experimental analysis of the tensile property of FFF-printed elastomers, Polym. Test. (2020). https://doi.org/10.1016/j.polymertesting.2020.106687.

[49] J.D. Gander, A. Jeffrey Giacomin, Review of die lip buildup in plastics extrusion, Polym. Eng. Sci. (1997). https://doi.org/10.1002/pen.11756.

[50] J.E. Seppala, S.H. Han, K.E. Hillgartner, C.S. Davis, K.B. Migler, Weld formation during material extrusion additive manufacturing, Soft Matter. 13 (2017) 6761–6769. https://doi.org/10.1039/c7sm00950j.

[51] W.P. Cox, E.H. Merz, Correlation of dynamic and steady flow viscosities, J. Polym. Sci. (1958). https://doi.org/10.1002/pol.1958.1202811812.

[52] Moldex 3D data bank, Moldex 3D. (2019).

[53] E. Sirjani, M. Migas, P.J. Cragg, M.K. Dymond, 3D printed UV/VIS detection systems constructed from transparent filaments and immobilised enzymes, Addit. Manuf. (2020). https://doi.org/10.1016/j.addma.2020.101094.

[54] S. B. Gandhi, 3D Printing of Transparent Materials For Optical Applications, 2018.

[55] B. Huang, S. Singamneni, Raster angle mechanics in fused deposition modelling, J. Compos. Mater. 49 (2015) 363–383. https://doi.org/10.1177/0021998313519153.

[56] S. Kain, J. V. Ecker, A. Haider, M. Musso, A. Petutschnigg, Effects of the infill pattern on mechanical properties of fused layer modeling (FLM) 3D printed wood/polylactic acid (PLA) composites, Eur. J. Wood Wood Prod. 78 (2020) 65–74. https://doi.org/10.1007/s00107-019-01473-0.

[57] D. Jiang, D.E. Smith, Anisotropic mechanical properties of oriented carbon fiber filled polymer composites produced with fused filament fabrication, Addit. Manuf. 18 (2017) 84–94. https://doi.org/10.1016/j.addma.2017.08.006.

[58] C. McIlroy, P.D. Olmsted, Deformation of an Amorphous Polymer during the Fused-Filament-Fabrication Method for Additive Manufacturing, J. Rheol. (N. Y. N. Y). 61 (2017) 379.

[59] H.R. Vanaei, K. Raissi, M. Deligant, M. Shirinbayan, J. Fitoussi, S. Khelladi, A. Tcharkhtchi, Toward the understanding of temperature effect on bonding strength, dimensions and geometry of 3D-printed parts, J. Mater. Sci. (2020). https://doi.org/10.1007/s10853-020-05057-9.

[60] W. Frellmann, S. Seidler, Deformation and Fracture Behaviour of Polymers, in: Deform. Fract. Behav. Polym., 2001. https://doi.org/10.1007/978-3-662-04556-5.

[61] B. Kuriakose, S.K. De, Scanning electron microscopy studies on tensile, tear and abrasion failure of thermoplastic elastomers, J. Mater. Sci. (1985). https://doi.org/10.1007/BF00555295.

[62] A.R. Torrado, C.M. Shemelya, J.D. English, Y. Lin, R.B. Wicker, D.A. Roberson, Characterizing the effect of additives to ABS on the mechanical property anisotropy of specimens fabricated by material extrusion 3D printing, Addit. Manuf. (2015). https://doi.org/10.1016/j.addma.2015.02.001.

[63] G. Cicala, D. Giordano, C. Tosto, G. Filippone, A. Recca, I. Blanco, Polylactide (PLA) filaments a biobased solution for additive manufacturing: Correlating rheology and thermomechanical properties with printing quality, Materials (Basel). (2018). https://doi.org/10.3390/ma11071191.

[64] M.A. Ryder, D.A. Lados, G.S. Iannacchione, A.M. Peterson, Fabrication and properties of novel polymer-metal composites using fused deposition modeling, Compos. Sci. Technol. 158 (2018) 43–50. https://doi.org/10.1016/j.compscitech.2018.01.049.

[65] C.G. Schirmeister, T. Hees, E.H. Licht, R. Mülhaupt, 3D printing of high density polyethylene by fused filament fabrication, Addit. Manuf. (2019). https://doi.org/10.1016/j.addma.2019.05.003.

[66] C. Koch, L. Van Hulle, N. Rudolph, Investigation of mechanical anisotropy of the fused filament fabrication process via customized tool path generation, Addit. Manuf. (2017). https://doi.org/10.1016/j.addma.2017.06.003.

[67] C. McIlroy, R.S. Graham, Modelling flow-enhanced crystallisation during fused filament fabrication of semi-crystalline polymer melts, Addit. Manuf. 24 (2018) 323–340. https://doi.org/10.1016/j.addma.2018.10.018.

[68] A. D'Amico, A.M. Peterson, An adaptable FEA simulation of material extrusion additive manufacturing heat transfer in 3D, Addit. Manuf. (2018). https://doi.org/10.1016/j.addma.2018.02.021.